Spin-Orbit Photonics in a Fixed Cavity: Harnessing Bogoliubov Modes of a Bose–Einstein Condensate

Muqaddar Abbas,[1,*] Ghaisud Din,[1] and Pei Zhang[1,†]

[1]Ministry of Education Key Laboratory for Nonequilibrium Synthesis and Modulation of Condensed Matter, Shaanxi Province Key Laboratory of Quantum Information and Quantum Optoelectronic Devices, School of Physics, Xi'an Jiaotong University, Xi'an 710049, China

We present a theoretical investigation of spin-orbit photonics within a fixed mirror cavity system containing a Bose-Einstein condensate (BEC), in which the Bogoliubov excitation modes of the condensate are treated as effective mechanical oscillators. By embedding the condensate in a single-mode optical cavity, we explore the emergence and modulation of the photonic spin Hall effect through the spin-dependent transverse shifts of a weak probe field. The optical response—encoded in the real and imaginary components of the output field susceptibility—is systematically analyzed as a function of the condensate–cavity coupling strength, revealing a controllable enhancement or suppression of the spin-orbit interaction. Our model captures how the interplay between collective BEC excitations and cavity photon dynamics induces nontrivial modifications in spin-dependent light propagation. Notably, we uncover that the Bogoliubov mode coupling acts as a tunable channel for mediating spin angular momentum transfer within the cavity, offering a novel route for engineering compact, quantum-coherent spin-orbit photonic devices.

I. INTRODUCTION

The photonic Spin Hall Effect (SHE) is a prominent manifestation of spin–orbit coupling (SOC) in optical systems, giving rise to a polarization-dependent lateral displacement of light at material interfaces [1]. This spatial splitting occurs due to the intrinsic interaction between the spin angular momentum of photons (associated with polarization) and their orbital trajectory, paralleling the spin Hall effect in electronic systems [2]. In such a photonic analogue, variations in the refractive index emulate the role of an electric field, producing a transverse shift that depends on the circular polarization components of the incident beam [1, 3, 4].

The theoretical basis for the photonic SHE was first established by Onoda *et al.* [1], with subsequent advancements contributed by Bliokh and co-authors, who offered a deeper understanding through conservation laws and geometric phase considerations [3]. Experimental verification was achieved in 2008 by Hosten and Kwiat via weak measurement protocols, enabling direct observation of the tiny polarization-induced beam shifts [5].

At its core, the photonic SHE arises from the conservation of total angular momentum in light–matter interactions, serving as a vital probe of spin–orbit phenomena in structured and inhomogeneous media [2, 6]. Techniques such as weak value amplification have proven highly effective in detecting the subtle spin-dependent displacements, significantly boosting the sensitivity of optical measurements [7, 8]. The broad utility of this effect has made it a cornerstone for numerous applications, ranging from precision metrology and quantum photonic devices to high-resolution optical imaging and sensor development [9–11].

* muqaddarabbas@xjtu.edu.cn
† zhangpei@mail.ustc.edu.cn

Recent advancements in light–matter interaction have laid the foundation for the development of highly controllable quantum optical platforms, enabling precise manipulation of photonic and atomic degrees of freedom [12–15]. Within this context, Bose-Einstein condensate (BECs) have emerged as exemplary quantum many-body systems, exhibiting macroscopic coherence and distinct superfluid properties that set them apart from conventional phases of matter [16]. The experimental realization of BECs in ultracold dilute gases has catalyzed major progress in quantum optics and quantum simulation [17, 18], offering deep insights into quantum phase transitions, long-range coherence, and collective excitations [19–21].

The integration of BECs with high-finesse optical cavities has opened new frontiers for investigating hybrid quantum systems, where the collective motion of ultracold atoms strongly couples to quantized cavity modes [22, 23]. These platforms allow the exploration of self-organized phases [24], cavity-mediated superradiance [25], and nontrivial optical nonlinearities in the few-photon regime [26]. Notably, the condensate's low-energy excitation spectrum—particularly the Bogoliubov modes—exhibits behavior analogous to mechanical oscillators [27–29]. These quasi-particle excitations, being sensitive to cavity field fluctuations, introduce a new optomechanical degree of freedom that is both tunable and coherent.

Consequently, the BEC can be viewed not only as a quantum fluid but also as a dynamic mechanical element in cavity optomechanics. This dual nature enables light-induced manipulation of condensate excitations and reciprocal modulation of the intracavity field. The bidirectional coupling between the BEC and the photonic field has been corroborated by theoretical and experimental investigations, revealing significant modifications to the system's optical susceptibility and quantum noise characteristics [16, 30]. In this work, we harness these properties to study spin-orbit photonic phenomena—specifically, the photonic spin Hall effect—within a static cavity-BEC system, wherein Bogoliubov modes serve as mechanically active channels for mediating spin-dependent light propagation.

In this work, we theoretically investigate a hybrid cavity quantum electrodynamics system in which a BEC, confined within a fixed-mirror optical cavity, serves as an effective mechanical oscillator via its Bogoliubov excitation modes. Our focus lies in exploring how the spin–orbit interaction of light, manifested through the photonic SHE, is influenced by the dynamical coupling between the quantized intracavity field and the collective modes of the condensate. By analyzing the real and imaginary parts of the output probe field susceptibility, we characterize the spin-dependent light shifts induced by this coupling and elucidate the conditions under which spin-orbit photonic effects can be enhanced or suppressed. The role of the effective optomechanical interaction strength is examined in detail, revealing its impact on the photonic SHE signature. This study provides new insight into the coherent control of spin–orbit photonic phenomena using quantum fluids of light and matter, offering potential avenues for the realization of tunable, compact spin-sensitive photonic devices based on atomic condensates.

II. Theoretical Model and Physical Configuration

We consider a hybrid optical system consisting of a BEC of N ultracold ^{87}Rb atoms confined inside an optical resonator, as shown in Fig. 1. A weak probe laser field, incident at an angle θ_{inc} on the partially reflective mirror M_1, interrogates the system. The probe beam has both transverse electric (TE) and transverse magnetic (TM) polarization components, with frequency ω_{P} and power P_{P}. The electric field amplitude is given by $|E_{\text{P}}| = \sqrt{\frac{2\kappa \text{P}_{\text{P}}}{\hbar\omega_{\text{P}}}}$, where κ denotes the cavity decay rate. Additionally, the cavity is coherently driven by a pump laser of frequency ω_{L} and power P_{L}, with amplitude $|E_{\text{L}}| = \sqrt{\frac{2\kappa \text{P}_{\text{L}}}{\hbar\omega_{\text{L}}}}$.

Upon reflection, the orthogonal circular polarization components of the probe field undergo a spatial separation transverse to the plane of incidence, indicative of the photonic spin Hall effect (SHE), as illustrated in Fig. 1.

To model this interaction, we use the transfer matrix formalism for the i^{th} layer of the three-layer system [31, 32]:

$$\mathcal{M}_i(k_x, \omega_p, d_i) = \begin{pmatrix} \cos(k_z^i) & \frac{i\sin(k_z^i)}{q_{is}} \\ iq_{is}\sin(k_z^i) & \cos(k_z^i) \end{pmatrix}, \tag{1}$$

where $k_z^i = d_i\sqrt{\epsilon_i k^2 - k^2\sin^2\theta}$ is the longitudinal wave vector component in the i^{th} layer of thickness d_i, and $q_{is} = \sqrt{\epsilon_i k^2 - k^2\sin^2\theta}$ characterizes the TE polarization. The complete transfer matrix for the multilayer system is given by:

$$y(k_x, \omega_p) = \mathcal{M}_1\mathcal{M}_2\mathcal{M}_3. \tag{2}$$

The reflection coefficients for TE and TM polarization are:

$$R_s = \frac{q_{1s}(y_{11} + y_{12}q_{3s}) - (q_{3s}y_{22} + y_{21})}{q_{1s}(y_{11} + y_{12}q_{3s}) + (q_{3s}y_{22} + y_{21})}, \tag{3}$$

$$R_p = \frac{p_{1m}(y_{11} + y_{12}p_{3m}) - (p_{3m}y_{22} + y_{21})}{p_{1m}(y_{11} + y_{12}p_{3m}) + (p_{3m}y_{22} + y_{21})}. \tag{4}$$

For a spatially localized Gaussian probe beam, the electric field amplitudes of the reflected left- and right-handed circularly polarized components are:

$$\begin{aligned}\mathcal{E}_r^{\pm}(x_r, y_r, z_r) = \frac{\omega_0}{\omega}\exp\left[-\frac{x_r^2 + y_r^2}{\omega}\right] \\ \times\left[R_p - \frac{2ix_r}{k\omega}\frac{\partial R_p}{\partial\theta} \mp \frac{2y_r\cot\theta}{k\omega}(R_s + R_p)\right].\end{aligned} \tag{5}$$

The transverse spatial shift of each spin component due to the photonic SHE is calculated as:

$$\delta_p^{\pm} = \frac{\int y|\mathcal{E}_r^{\pm}(x_r, y_r, z_r)|^2\, dx_r dy_r}{\int |\mathcal{E}_r^{\pm}(x_r, y_r, z_r)|^2\, dx_r dy_r}. \tag{6}$$

Substituting Eq. (5) into Eq. (6) yields the spin-dependent displacement:

$$\delta_p^{\pm} = \mp\frac{k_1\omega_0^2\,\text{Re}\left[1 + \frac{R_s}{R_p}\right]\cot\theta_i}{k_1^2\omega_0^2 + \left|\frac{\partial\ln R_p}{\partial\theta_i}\right|^2 + \left|\left(1 + \frac{R_s}{R_p}\right)\cot\theta_i\right|^2}. \tag{7}$$

The shift δ_p^+ and δ_p^- represent the left- and right-circular polarization, respectively, with equal magnitude but opposite direction due to symmetry. The permittivity of the intracavity BEC medium, ϵ_2, is crucial in determining the shift, where $\epsilon_2 = 1 + \chi$ and χ is the effective susceptibility.

To compute χ, we use the quantum Langevin formalism and input-output theory [33], with χ proportional to the steady-state output field amplitude, i.e., $\chi = E_{\text{T}}$.

In the next section, we derive the susceptibility by solving the coupled quantum equations of motion for the system dynamics.

III. System Hamiltonian and Dynamics of a BEC-Cavity Coupled System

We consider a hybrid quantum system comprising a BEC interacting with a single-mode optical cavity. The full Hamiltonian of the system is given by:

$$\begin{aligned}\mathscr{H} = &\int \mathrm{d}x\,\Psi^\dagger(x)\left[-\frac{\hbar^2}{2m}\frac{\mathrm{d}^2}{\mathrm{d}x^2} + V_{\text{ext}}(x) + \hbar U_0\cos^2(kx)\,a^\dagger a\right] \\ &\Psi(x) + \hbar\omega_a\,a^\dagger a + i\hbar E_L(a^\dagger e^{-i\omega_L t} - a\,e^{i\omega_L t}) \\ &+ i\hbar E_P(a^\dagger e^{-i\omega_P t} - a\,e^{i\omega_P t})\end{aligned} \tag{8}$$

Here, $\Psi^\dagger(x)$ and $a^\dagger$ denote the bosonic creation operators for the atomic field and cavity photons, respectively.

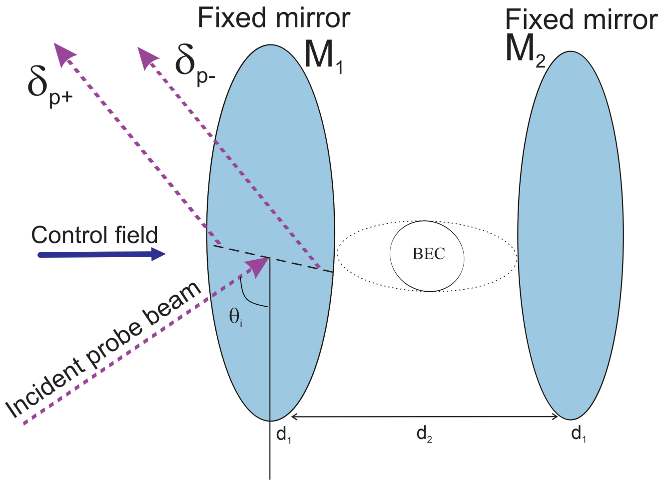

FIG. 1. The schematic of the cavity system is shown, which includes a BEC of N ^{87}Rb atoms and OPA. The red arrows represent the incoming and outgoing probe light from the left mirror M_1 with an incident angle θ_{inc}. The black arrows indicate the control field, while $\mathrm{S_r}$ denotes the shift in the reflected probe light. Both cavity mirrors, M_1 and M_2, are fixed in place.

The cavity mode profile is described by $\cos(kx)$, where $k = 2\pi/\lambda$ is the optical wave vector. The atom-induced dispersive shift is characterized by $U_0 = g_0^2/\Delta_a$, with g_0 being the atom-cavity coupling and Δ_a the atom–cavity detuning. The coherent driving by lasers at frequencies ω_L and ω_P is introduced through amplitudes E_L and E_P.

Moving into the rotating frame at ω_L and applying the Bogoliubov approximation for atomic excitations, the Hamiltonian simplifies to:

$$\begin{aligned}\mathcal{H} &= \hbar\Delta_a\, a^\dagger a + \hbar\omega_m\, b^\dagger b + \hbar g_{bc}\, a^\dagger a(b + b^\dagger) \\ &\quad + i\hbar E_L(a^\dagger - a) + i\hbar E_P\left(a^\dagger e^{-i\delta t} - a e^{i\delta t}\right),\end{aligned} \tag{9}$$

where $\Delta_a = \omega_a + \frac{U_0 N}{2} - \omega_L$ includes the mean-field shift from N atoms, $\omega_m = 4\omega_{\mathrm{rec}}$ is the Bogoliubov mode frequency with $\omega_{\mathrm{rec}} = \hbar k^2/2m$, and $g_{bc} = \frac{U_0}{2}\sqrt{N/2}$ represents the effective optomechanical coupling. The final two terms represent the interaction between the cavity and the external driving fields: the pump and probe lasers, characterized by a detuning $\delta = \omega_P - \omega_L$ between the pump and probe frequencies.

Including damping and quantum noise, the Heisenberg-Langevin equations for the cavity and mechanical modes are:

$$\dot{a} = -\left(i\Delta_a + \kappa\right) a - i g_{bc}\, a(b + b^\dagger) + E_L + E_P\, e^{-i\delta t} \tag{10}$$

$$+ \sqrt{2\kappa}\, a_{\mathrm{in}}, \tag{11}$$

$$\dot{b} = -\left(i\omega_m + \gamma_m\right) b - i g_{bc}\, a^\dagger a + \sqrt{2\gamma_m}\, \xi, \tag{12}$$

where κ and γ_m are the cavity and mechanical damping rates, and a_{in}, ξ are input noise operators.

Expanding around steady-state values $a = \alpha + \delta a$, $b = \beta + \delta b$, and retaining only first-order fluctuations yields:

$$\delta\dot{a} = -\left(i\Delta + \kappa\right)\delta a - i G_{\mathrm{BC}}\left(\delta b + \delta b^\dagger\right) + E_P\, e^{-i\delta t}, \tag{13}$$

$$\delta\dot{b} = -\left(i\omega_m + \gamma_m\right)\delta b - i G_{\mathrm{BC}}\,\delta a^\dagger - i G_{\mathrm{BC}}^*\,\delta a, \tag{14}$$

with $G_{\mathrm{BC}} = g_{bc}|\alpha|$ and $\Delta = \Delta_a - g_{bc}(\beta + \beta^*)$ is the effective detuning.

The steady-state intracavity amplitudes are given by:

$$\alpha = \frac{E_L(\kappa - i\Delta)}{\kappa^2 + \Delta^2}, \tag{15}$$

$$\beta = -\frac{i g_{bc}|\alpha|^2}{i\omega_m + \gamma_m}. \tag{16}$$

To study the probe response, we adopt the ansatz:

$$\delta a(t) = \delta a_- e^{-i\delta t} + \delta a_+ e^{i\delta t}, \tag{17}$$

$$\delta b(t) = \delta b_- e^{-i\delta t} + \delta b_+ e^{i\delta t}. \tag{18}$$

Substituting into Eqs. (13)–(14) and solving algebraically, the total cavity output field reads:

$$E_{\mathrm{out}}(t) + E_P e^{-i\delta t} + E_L = \sqrt{2\kappa}\, a(t), \tag{19}$$

where the output probe signal is decomposed as:

$$E_{\mathrm{out}}(t) = E_{\mathrm{out}}^{(0)} + E_{\mathrm{out}}^{(+)} E_P e^{-i\delta t} + E_{\mathrm{out}}^{(-)} E_P e^{i\delta t}. \tag{20}$$

The probe transmission is then characterized by:

$$E_{\mathrm{out}}^{(+)} = \frac{\sqrt{2\kappa}\, a_-}{E_P} - 1, \tag{21}$$

$$E_T = \frac{\sqrt{2\kappa}\, a_-}{E_P}, \tag{22}$$

where a_- is the intracavity response to the probe field, obtained as:

$$a_- = \frac{\mathcal{A}}{\mathcal{B}}, \tag{23}$$

with:

$$\begin{aligned}\mathcal{A} = -E_P\Big[&2iG_{\mathrm{BC}}^2\omega_{\mathrm{m}} + (\gamma_{\mathrm{m}} - i\Delta_{\mathbb{P}})(\gamma_{\mathrm{m}} - i(\Delta_{\mathbb{P}} + 2\omega_{\mathrm{m}})) \\ &\times(\kappa - i(\Delta_{\mathbb{P}} + 2\omega_{\mathrm{m}}))\Big]\end{aligned} \tag{24}$$

$$\begin{aligned}\mathcal{B} = (\kappa - i\Lambda)\Big[&-2iG_{\mathrm{BC}}^2\omega_{\mathrm{m}} + (\gamma_{\mathrm{m}} - i\Delta_{\mathbb{P}})(i\gamma_{\mathrm{m}} + \Delta_{\mathbb{P}} + 2\omega_{\mathrm{m}}) \\ &\times(i\kappa + \Delta_{\mathbb{P}} + 2\omega_{\mathrm{m}})\Big] - 2G_{\mathrm{BC}}\left(-i\kappa - \Delta_{\mathbb{P}} - 2\omega_{\mathrm{m}}\right)\omega_{\mathrm{m}}\, G_{\mathrm{BC}}^*.\end{aligned} \tag{25}$$

In the resolved sideband limit, where $\omega_m \gg \kappa$ and the detuning is set to $\Delta = \omega_m$, the term $\Delta_{\mathbb{P}} = \delta - \omega_m$ in the previous expression represents the detuning relative to the central frequency of the sideband. The transmission of the probe E_T effectively serves as the susceptibility χ of the intra-cavity medium, that is, $\chi = \chi_r + i\chi_i \equiv E_T$. Both real and imaginary parts of χ determine the phase and absorption response of the system, respectively, and can be accessed via homodyne detection techniques.

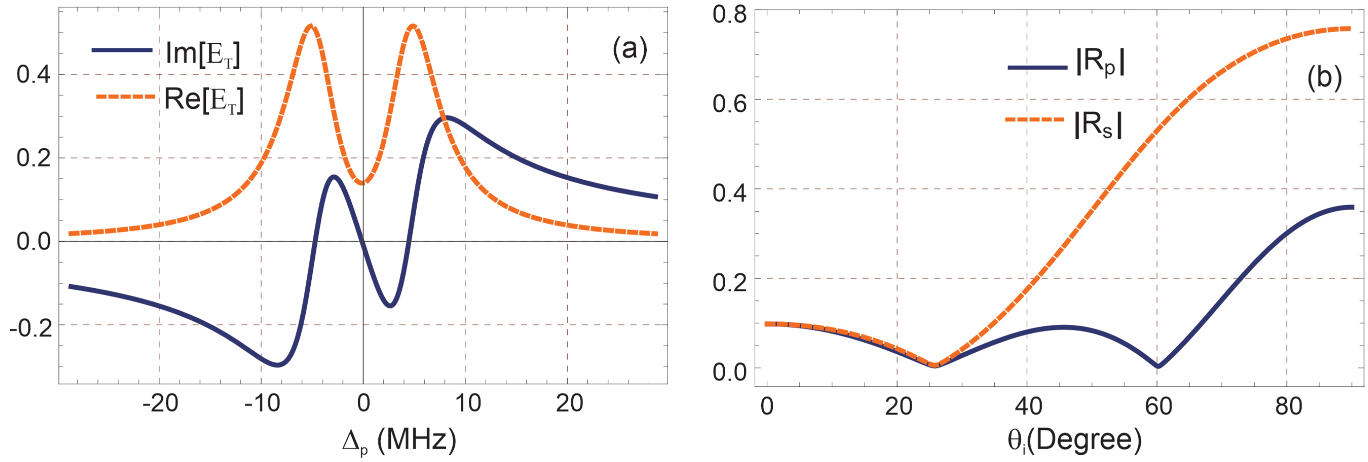

FIG. 2. (a) Dispersion (solid curve) and absorption (dashed curve) characteristics of the intracavity BEC system as functions of the probe field detuning Δ_p, evaluated at $\omega_{\rm m}/2\pi = 15.2$ kHz, $\gamma_{\rm m}/2\pi = 0.21$ kHz, $\omega_{\rm rec}/2\pi = 3.8$ kHz, $\lambda = 780$ nm, $L = 1.25\times10^{-4}$ m, $\mathrm{G_{BC}} = 0.05\omega_{\rm m}$, and cavity decay $\kappa = 0.05\omega_m$. (b) Variation of the Fresnel reflection coefficients $|R_s|$ and $|R_p|$ with the incident angle θ_i. In panel (b), we consider resonant probe field detuning $\Delta_p = 0$. The remaining parameters are $\epsilon_0 = 1$, $\epsilon_1 = \epsilon_3 = 2.22$, $\epsilon_2 = 1 + E_T$, mirror thicknesses $d_1 = 0.1\times10^{-6}$ m and $d_2 = 0.4\times10^{-6}$ m.

IV. RESULTS AND DISCUSSION

We employ experimentally feasible parameters [34, 35] $\omega_{\rm m}/2\pi = 15.2$kHz, $\gamma_{\rm m}/2\pi = 0.21$kHz, $\omega_{rec}/2\pi = 3.8$kHz, $\lambda = 780$nm, L $= 1.25\times10^{-4}$m. For the GHS we use additional parameters $\epsilon_0 = 1$, $\epsilon_1 = \epsilon_3 = 2.22$, mirror thickness $\mathrm{d_1} = 0.2\times10^{-6}$m, $\mathrm{d_2} = 5\times10^{-6}$m.

Figure 2 presents a comprehensive analysis of the optical response of the intracavity BEC system. In panel (a), we plot the dispersion (real part of the susceptibility, solid curve) and absorption (imaginary part of the susceptibility, dashed curve) as functions of the probe field detuning Δ_p, using experimentally realizable parameters: mechanical frequency $\omega_{\rm m}/2\pi = 15.2$ kHz, mechanical damping $\gamma_{\rm m}/2\pi = 0.21$ kHz, recoil frequency $\omega_{\rm rec}/2\pi = 3.8$ kHz, and cavity length $L = 1.25\times10^{-4}$ m. The light–matter interaction strength is governed by the BEC–cavity coupling $G_{\rm BC} = 0.05\omega_{\rm m}$ and cavity decay rate $\kappa = 0.05\omega_{\rm m}$.

The dispersion curve exhibits a steep slope in the vicinity of $\Delta_p = 0$, signifying strong group velocity dispersion indicative of slow-light effects. This region corresponds to a rapid variation of the refractive index, a consequence of coherent interference within the hybrid cavity–BEC system. Meanwhile, the absorption profile displays a pronounced transparency window near resonance, suggesting the presence of an electromagnetically induced transparency (EIT)-like phenomenon. This behavior emerges due to destructive interference between different excitation pathways in the coupled light–matter system, effectively suppressing absorption at exact resonance.

In panel (b), we examine the angular dependence of the Fresnel reflection coefficients $|R_s|$ and $|R_p|$ under resonant probe field detuning $\Delta_p = 0$. The dielectric environment comprises layers with permittivities $\epsilon_0 = 1$, $\epsilon_1 = \epsilon_3 = 2.22$, and $\epsilon_2 = 1 + E_T$, where E_T represents a tunable external control parameter. The multilayer stack includes mirror thicknesses $d_1 = 0.1\times10^{-6}$ m and $d_2 = 0.4\times10^{-6}$ m.

The results show that $|R_p|$ displays a dip around the Brewster angle, a classical effect arising from zero reflectivity for p-polarized light at a specific angle of incidence. In contrast, $|R_s|$ remains finite and comparatively flat across the angular spectrum, reflecting its insensitivity to such Brewster-angle effects. The sharp angular contrast between the two polarizations establishes a favorable condition for spin-dependent optical phenomena, such as the photonic PSHE, where the angular separation of spin components is maximized.

These findings confirm that the system supports tunable dispersion and polarization-selective reflection, essential for tailoring light propagation, enhancing light–matter interactions, and enabling spin-dependent optical control. The tunability via Δ_p and θ_i, along with the engineered dielectric environment, underscores the potential of this platform for applications in slow-light devices, precision sensing, and spin-resolved photonic interfaces.

To explore the polarization-dependent response of the system, we analyze the ratio $|R_s|/|R_p|$ of the reflection amplitudes for s- and p-polarized components as a function of the incident angle θ_i for various probe field detunings Δ_p, as shown in Figure **??**. The calculations are carried out using experimentally feasible parameters: mechanical frequency $\omega_{\rm m}/2\pi = 15.2$ kHz, mechanical damping $\gamma_{\rm m}/2\pi = 0.21$ kHz, recoil frequency $\omega_{\rm rec}/2\pi =$ 3.8 kHz, and optical wavelength $\lambda = 780$ nm. The optical cavity is characterized by length $L = 1.25\times10^{-4}$ m, coupling strength $G_{\rm BC} = 0.05\omega_{\rm m}$, and cavity decay rate $\kappa = 0.05\omega_{\rm m}$, with the dielectric structure defined by permittivities $\epsilon_0 = 1$, $\epsilon_1 = \epsilon_3 = 2.22$, and $\epsilon_2 = 1 + E_T$, where E_T denotes the tunable component related to ex-

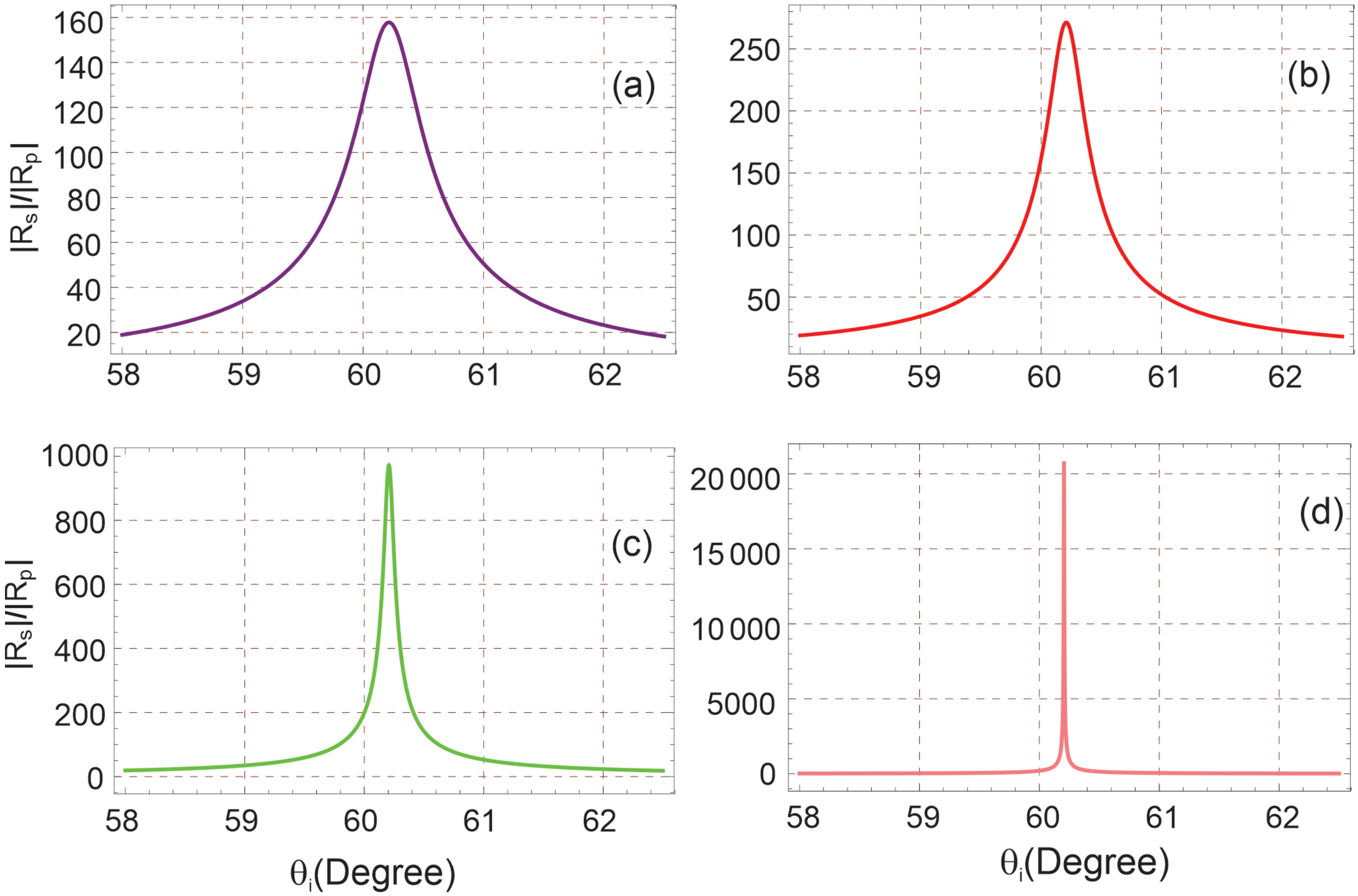

FIG. 3. Ratio $|R_s|/|R_p|$ as a function of the incident angle θ_i for different values of the probe field detuning: (a) $\Delta_p = 0$, (b) $\Delta_p = -0.05\omega_\mathrm{m}$, (c) $\Delta_p = -0.1\omega_\mathrm{m}$, and (d) $\Delta_p = -0.12\omega_\mathrm{m}$. The remaining parameters are $\omega_\mathrm{m}/2\pi = 15.2$ kHz, $\gamma_\mathrm{m}/2\pi = 0.21$ kHz, $\omega_\mathrm{rec}/2\pi = 3.8$ kHz, $\lambda = 780$ nm, $L = 1.25 \times 10^{-4}$ m, $\mathrm{G_{BC}} = 0.05\omega_\mathrm{m}$, $\kappa = 0.05\omega_m$, $\epsilon_0 = 1$, $\epsilon_1 = \epsilon_3 = 2.22$, $\epsilon_2 = 1 + E_T$, mirror thicknesses $d_1 = 0.1 \times 10^{-6}$ m and $d_2 = 0.4 \times 10^{-6}$ m.

ternal bias. The thicknesses of the dielectric layers are fixed at $d_1 = 0.1 \times 10^{-6}$ m and $d_2 = 0.4 \times 10^{-6}$ m.

Figure 3(a)–(d) correspond to detuning values $\Delta_p = 0$, $-0.05\omega_\mathrm{m}$, $-0.1\omega_\mathrm{m}$, and $-0.12\omega_\mathrm{m}$, respectively. For $\Delta_p = 0$, the ratio $|R_s|/|R_p|$ exhibits a moderate angular variation near $\theta_i \approx 60.2^\circ$, indicating a baseline scenario where spin-dependent reflection is balanced. As the detuning becomes increasingly negative, a pronounced asymmetry develops in the angular profile of the ratio. Specifically, for $\Delta_p = -0.05\omega_\mathrm{m}$, the ratio sharply increases near resonance, showing enhanced reflection for one polarization component relative to the other.

Further increasing the detuning to $\Delta_p = -0.1\omega_\mathrm{m}$ and $-0.12\omega_\mathrm{m}$ leads to a more substantial amplification in the peak value of $|R_s|/|R_p|$, accompanied by a narrowing angular window around the resonance angle. This behavior is attributed to the enhanced spin–orbit interaction in the detuned regime, where the probe field selectively couples to spin-polarized modes within the cavity–BEC hybrid system. The detuning effectively modifies the optical susceptibility experienced by each polarization component, resulting in distinct reflection amplitudes.

These findings highlight the critical role of probe detuning in engineering polarization selectivity. By tuning Δ_p, one can modulate the angular and spectral response of the reflected field, enabling dynamic control over polarization-based filtering and sensing. The observed resonant enhancement and tunability of $|R_s|/|R_p|$ establish this configuration as a promising candidate for spin-resolved photonic devices and quantum optical interfaces.

Figure 4 explores the behavior of the normalized photonic spin Hall effect (SHE) shift, δ_r^+/λ, as a function of the incident angle θ_i, with emphasis on the influence of probe field detuning Δ_p. In panel (a), four representative values of Δ_p are considered, while panel (b) presents a density map of δ_r^+/λ in the (θ_i, Δ_p) parameter space.

In Figure 4(a), it is evident that the SHE shift exhibits a sharp resonant feature around $\theta_i \approx 60.2^\circ$. The nature and magnitude of this resonance are highly sensitive to the probe detuning. When $\Delta_p = 0$ (red dashed line), a symmetric Lorentzian-like peak is observed, indicating strong spin-dependent angular deflection due to enhanced light–matter interaction at zero detuning. As

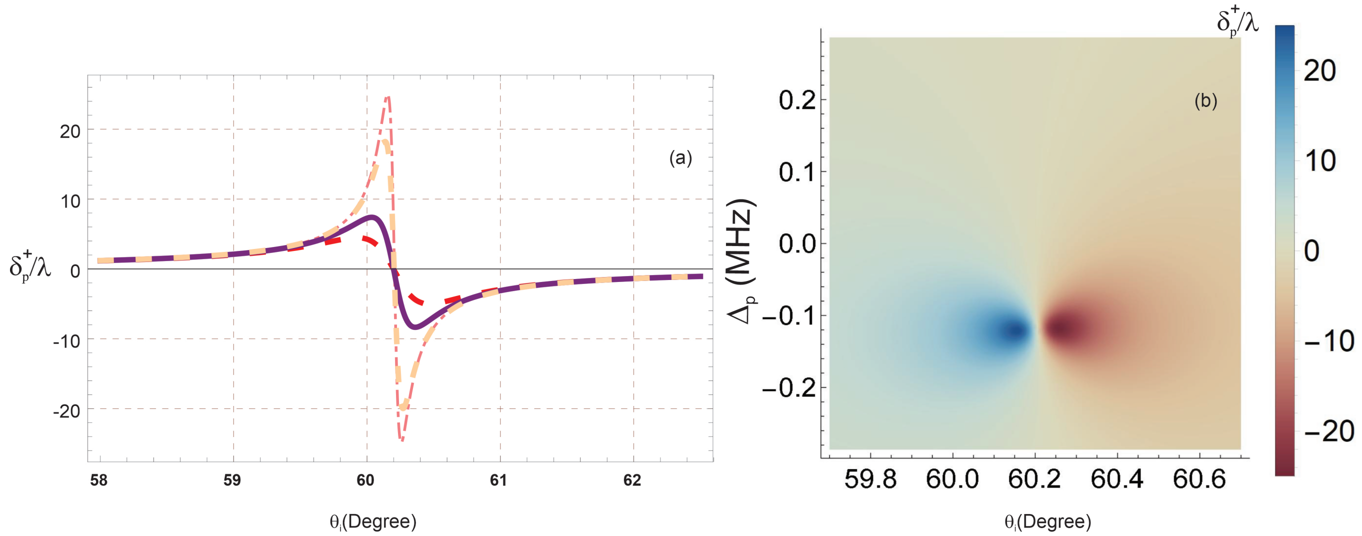

FIG. 4. (a) Normalized photonic SHE shift δ_p^+/λ as a function of the incident angle θ_i for different values of the probe field detuning: $\Delta_p = 0$ (red dashed line), $\Delta_p = -0.05\omega_\mathrm{m}$ (purple solid line), $\Delta_p = -0.1\omega_\mathrm{m}$ (off-white dashed line), and $\Delta_p = -0.12\omega_\mathrm{m}$ (pink dot dashed line). (b) Density plot of photonic SHE shift δ_p^+/λ as a function of the incident angle θ_i and detuning of probe field Δ_p. The remaining parameters are $\omega_\mathrm{m}/2\pi = 15.2$ kHz, $\gamma_\mathrm{m}/2\pi = 0.21$ kHz, $\omega_\mathrm{rec}/2\pi = 3.8$ kHz, $\lambda = 780$ nm, $L = 1.25 \times 10^{-4}$ m, $\mathrm{G_{BC}} = 0.05\omega_\mathrm{m}$, $\kappa = 0.05\omega_m$, $\epsilon_0 = 1$, $\epsilon_1 = \epsilon_3 = 2.22$, $\epsilon_2 = 1 + E_T$, mirror thicknesses $d_1 = 0.1 \times 10^{-6}$ m and $d_2 = 0.4 \times 10^{-6}$ m.

the probe detuning becomes increasingly negative, e.g., $\Delta_p = -0.05\omega_m$ (purple solid line), $-0.10\omega_m$ (off-white dashed line), and $-0.12\omega_m$ (pink dot-dashed line), the magnitude of the SHE shift increases, but the peak structure becomes increasingly asymmetric and broadened. This behavior signifies the onset of dispersive optical response, where the detuning modifies the effective refractive index and hence the spin–orbit interaction strength.

Panel (b) further confirms this trend through a two-dimensional density plot showing how δ_r^+/λ evolves over a range of incident angles and detuning values. A striking antisymmetric pattern emerges around $\theta_i \approx 60.2^\circ$ and $\Delta_p = 0$, with a strong transition from negative to positive shift values as one moves across this point. The blue and red lobes in the plot reflect the competing contributions of constructive and destructive interference between left- and right-circular polarization components, influenced by the detuning. The central dip-peak structure in the color map reinforces the idea that the system exhibits maximum spin sensitivity at near-resonant conditions.

The physical origin of the observed sensitivity lies in the detuning-dependent modification of the cavity–BEC hybrid mode dispersion. At resonance, the overlap between the photonic mode and the collective atomic excitation is maximized, leading to significant spin–orbit coupling and enhanced SHE. Off-resonant interactions, in contrast, reduce this overlap and thus suppress or alter the direction of the transverse spin shift.

These results indicate that precise control over probe detuning can be utilized to engineer the magnitude and sign of the photonic SHE shift. Such tunability offers a route for developing active optical components, including polarization-sensitive switches and quantum optical sensors, where detection and manipulation of spin-dependent beam shifts are essential.

Figure 5 illustrates the density plots of the normalized photonic spin Hall effect (SHE) shift, δ_r^+/λ, as a function of the incident angle θ_i and the cavity–BEC coupling strength G_BC, for two different cavity dissipation regimes. These regimes are defined by the relation between the cavity loss rate κ and the BEC damping rate γ_m. The plots are obtained using realistic system parameters, as detailed in the caption.

In panel (a), the condition $\kappa/2\pi = \gamma_m/2\pi = 0.21$ kHz is considered, which signifies balanced dissipation rates for the cavity and the BEC. Under this symmetric dissipation regime, a pronounced peak in the photonic SHE shift appears around $\theta_i \approx 59^\circ$, particularly for weak to moderate coupling strengths ($G_\mathrm{BC}/\omega_m \lesssim 10$). This behavior is attributed to the resonant enhancement of the light–matter interaction, where the photonic SHE is maximized due to efficient momentum transfer at the interface. The sharp color gradient near this angular region also highlights a strong angular sensitivity of the shift, making the system favorable for precision sensing applications.

In contrast, panel (b) presents the scenario where the cavity dissipation dominates ($\kappa = 0.5\omega_m$, while $\gamma_m/2\pi = 0.21$ kHz remains fixed). In this case, the overall magnitude of the normalized SHE shift increases compared to panel (a), with broader regions of significant positive values. The peak region shifts slightly to larger incident angles, and the SHE becomes less sharply localized in both angle and coupling strength. The enhancement in this

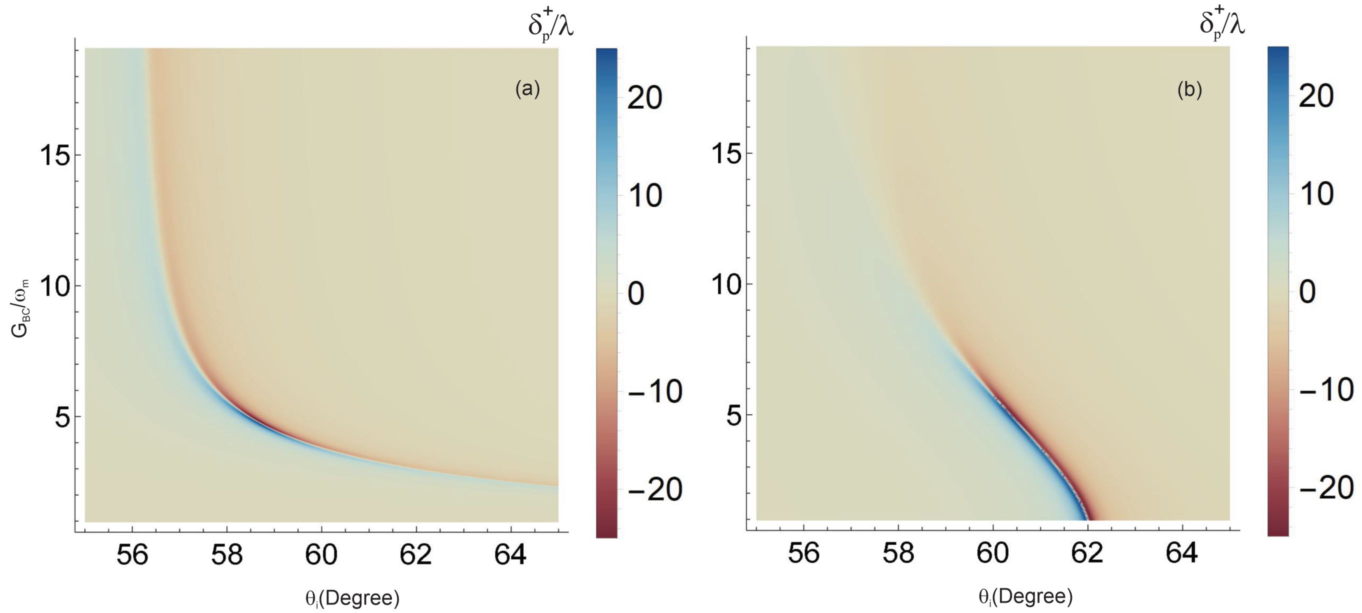

FIG. 5. Density plot of the normalized photonic spin Hall effect (SHE) shift, δ_p^+/λ, as a function of the incident angle θ_i and the cavity–BEC coupling strength $\mathrm{G_{BC}}$, for two dissipation regimes: (a) when the cavity dissipation rate κ equals the BEC dissipation rate γ_b, i.e., $\kappa/2\pi = \gamma_m/2\pi = 0.21$ kHz, and (b) when the cavity dissipation rate exceeds that of the BEC, i.e., $\kappa = 0.5\,\omega_m$ and $\gamma_m/2\pi = 0.21$ kHz. The remaining parameters are: probe detuning $\Delta_p = -0.12\,\omega_m$ (corresponding to the maximum photonic SHE), mechanical frequency $\omega_m/2\pi = 15.2$ kHz, recoil frequency $\omega_{\rm rec}/2\pi = 3.8$ kHz, wavelength $\lambda = 780$ nm, cavity length $L = 1.25 \times 10^{-4}$ m, dielectric constants $\epsilon_0 = 1$, $\epsilon_1 = \epsilon_3 = 2.22$, $\epsilon_2 = 1 + E_T$, mirror thicknesses $d_1 = 0.1 \times 10^{-6}$ m and $d_2 = 0.4 \times 10^{-6}$ m.

regime arises due to increased photonic leakage, which facilitates more efficient extraction of spin-dependent components of light, thus amplifying the observable SHE. However, the trade-off is a reduction in the quality factor of the cavity, which could limit coherence in certain quantum applications.

The comparison between panels (a) and (b) emphasizes the critical role of cavity dissipation in tailoring the photonic SHE. Specifically, by engineering the relative magnitudes of κ and γ_m, one can modulate the strength and angular profile of the SHE shift. This tunability is vital for designing reconfigurable photonic devices based on spin–orbit interaction, such as polarization-resolved sensors or optical switches.

Overall, the results confirm that optimal control of dissipation parameters and light–matter coupling enables precise manipulation of spin-dependent photonic transport, with potential applications in chiral quantum optics and topological photonics.

V. CONCLUSION

We have theoretically examined spin–orbit photonic phenomena in a fixed-mirror optical cavity system coupled to a BEC, where Bogoliubov excitation modes function as effective mechanical resonators. By embedding the BEC within a single-mode cavity, our model uncovers how spin-dependent light–matter interactions manifest as photonic SHE shifts of a weak probe beam, which are highly sensitive to system parameters.

The analysis reveals strong dispersive and absorptive responses around specific probe detunings, evidencing the role of the BEC–cavity interaction in modifying the system's optical transparency. The angular dependence of the Fresnel coefficients further supports the emergence of spin-selective scattering near the Brewster angle, establishing the angle-dependent origin of the photonic SHE.

Through systematic exploration of the ratio $|R_s|/|R_p|$ and the corresponding photonic SHE shift $\delta^{\star}_{+}/\lambda$, we demonstrate that the magnitude and sign of the transverse spin-dependent shift are strongly modulated by the probe field detuning. A critical enhancement of the photonic SHE occurs near resonance, highlighting the cavity-assisted control over the spin–orbit interaction channel. Additionally, the parameter regimes in which spin-orbit effects are maximized are clearly visualized through two-dimensional contour mappings.

Further insights establish how cavity dissipation governs the SHE response. In particular, under equal dissipation conditions for the cavity and the BEC ($\kappa = \gamma_m$), the shift profile becomes sharper and more localized, while higher cavity losses smooth out the transverse spin shift features. This illustrates the tunability of the spin–orbit effect via dissipative engineering.

Overall, our findings confirm that the interplay between Bogoliubov collective excitations and cavity photon dynamics not only mediates angular momentum exchange but also enables fine control over spin-dependent light steering. The BEC–cavity platform thus serves as a promising medium for developing reconfigurable, miniaturized spin–orbit photonic devices with potential applications in optical sensing, nonreciprocal signal processing, and quantum information routing.

Acknowledgements

This work was supported by the National Natural Science Foundation of China (Grant No. 12174301), the Young Investigator (Grant No. 12305027), the Natural Science Basic Research Program of Shaanxi (Program No. 2023-JC-JQ-01), and the Fundamental Research Funds for the Central Universities.

[1] M. Onoda, S. Murakami, and N. Nagaosa, Phys. Rev. Lett. **93**, 083901 (2004).

[2] K. Y. Bliokh, F. J. Rodríguez-Fortuño, F. Nori, and A. V. Zayats, Nat. Photonics **9**, 796 (2015).

[3] K. Y. Bliokh and Y. P. Bliokh, Phys. Rev. Lett. **96**, 073903 (2006).

[4] J. Sinova, S. O. Valenzuela, J. Wunderlich, C. Back, and T. Jungwirth, Rev. Mod. Phys. **87**, 1213 (2015).

[5] O. Hosten and P. Kwiat, Science **319**, 787 (2008).

[6] F. Cardano and L. Marrucci, Nat. Photonics **9**, 776 (2015).

[7] L. Cai, M. Liu, S. Chen, Y. Liu, W. Shu, H. Luo, and S. Wen, Phys. Rev. A **95**, 013809 (2017).

[8] S. Chen, X. Zhou, C. Mi, H. Luo, and S. Wen, Phys. Rev. A **91**, 062105 (2015).

[9] A. Aiello, N. Lindlein, C. Marquardt, and G. Leuchs, Phys. Rev. Lett. **103**, 100401 (2009).

[10] X. Yin, Z. Ye, J. Rho, Y. Wang, and X. Zhang, Science **339**, 1405 (2013).

[11] P. Dong, J. Xu, and J. Cheng, Phys. Plasmas **31** (2024).

[12] F. Badshah, M. Abbas, Y. Zhou, H. Huang, *et al.*, Optics & Laser Technology **182**, 112078 (2025).

[13] Y. Zhou, J.-W. Wang, L.-Z. Cao, G.-H. Wang, Z.-Y. Shi, D.-Y. Lü, H.-B. Huang, and C.-S. Hu, Reports on Progress in Physics **87**, 100502 (2024).

[14] F. Badshah, Y. Zhou, Z. Shi, H. Huang, Z. Ullah, and M. Idrees, Chinese Journal of Physics **92**, 1674 (2024).

[15] F. Badshah, S. Asghar, S.-H. Dong, *et al.*, Optics & Laser Technology **177**, 111104 (2024).

[16] F. Brennecke, S. Ritter, T. Donner, and T. Esslinger, Science **322**, 235 (2008).

[17] M. H. Anderson, J. R. Ensher, M. R. Matthews, C. E. Wieman, and E. A. Cornell, science **269**, 198 (1995).

[18] K. B. Davis, M. O. Mewes, M. R. Andrews, N. J. van Druten, D. S. Durfee, D. M. Kurn, and W. Ketterle, Phys. Rev. Lett. **75**, 3969 (1995).

[19] F. Dalfovo, S. Giorgini, L. P. Pitaevskii, and S. Stringari, Rev. Mod. Phys. **71**, 463 (1999).

[20] S. Botelho and C. S. d. Melo, Journal of low temperature physics **140**, 409 (2005).

[21] M. Aizenman, E. H. Lieb, R. Seiringer, J. P. Solovej, and J. Yngvason, Condensed Matter Physics and Exactly Soluble Models: Selecta of Elliott H. Lieb , 337 (2004).

[22] H. Ritsch, P. Domokos, F. Brennecke, and T. Esslinger, Rev. Mod. Phys. **85**, 553 (2013).

[23] I. B. Mekhov, C. Maschler, and H. Ritsch, Nature physics **3**, 319 (2007).

[24] K. Baumann, C. Guerlin, F. Brennecke, and T. Esslinger, nature **464**, 1301 (2010).

[25] Y. Chen, H. Zhai, and Z. Yu, Phys. Rev. A **91**, 021602 (2015).

[26] A. Dalafi and M. H. Naderi, Phys. Rev. A **95**, 043601 (2017).

[27] W. Chen, D. S. Goldbaum, M. Bhattacharya, and P. Meystre, Phys. Rev. A **81**, 053833 (2010).

[28] D. Nagy, P. Domokos, A. Vukics, and H. Ritsch, The European Physical Journal D **55**, 659 (2009).

[29] P. Horak and H. Ritsch, Phys. Rev. A **64**, 033422 (2001).

[30] C. Maschler and H. Ritsch, Phys. Rev. Lett. **95**, 260401 (2005).

[31] M. Born, E. Wolf, A. B. Bhatia, P. Clemmow, D. Gabor, A. Stokes, A. Taylor, P. Wayman, and W. Wilcock, *Principles of optics: electromagnetic theory of propagation, interference and diffraction of light*, Vol. 7 (Cambridge university press Cambridge, 1999).

[32] L. Wu, H.-S. Chu, W. S. Koh, and E.-P. Li, Opt. Express **18**, 14395 (2010).

[33] D. Walls and G. J. Milburn, in *Quantum Optics* (Springer, 2008) pp. 307–346.

[34] F. Brennecke, T. Donner, S. Ritter, T. Bourdel, M. Köhl, and T. Esslinger, nature **450**, 268 (2007).

[35] Y. Colombe, T. Steinmetz, G. Dubois, F. Linke, D. Hunger, and J. Reichel, Nature **450**, 272 (2007).